NANO LETTERS

Letter

pubs.acs.org/NanoLett

Self-Assembly of Colloidal Hexagonal Bipyramid- and Bifrustum-Shaped ZnS Nanocrystals into Two-Dimensional Superstructures

Ward van der Stam,[†] Anjan P. Gantapara,[§] Quinten A. Akkerman,[†] Giuseppe Soligno,[‡] Johannes D. Meeldijk,[⊥] René van Roij,[‡] Marjolein Dijkstra,*[,§] and Celso de Mello Donega*[,†]

[†]Condensed Matter and Interfaces and [§]Soft Condensed Matter, Debye Institute for Nanomaterials Science, Utrecht University, 3508 TA Utrecht, The Netherlands

[‡]Institute for Theoretical Physics, Utrecht University, Leuvenlaan 4, 3584 CE Utrecht, The Netherlands

[⊥]Electron Microscopy Utrecht, Utrecht University, 3584 CH Utrecht, The Netherlands

Supporting Information

ABSTRACT: We present a combined experimental, theoretical, and simulation study on the self-assembly of colloidal hexagonal bipyramid- and hexagonal bifrustum-shaped ZnS nanocrystals (NCs) into two-dimensional superlattices. The simulated NC superstructures are in good agreement with the experimental ones. This shows that the self-assembly process is primarily driven by minimization of the interfacial free-energies and maximization of the packing density. Our study shows that a small truncation of the hexagonal bipyramids is sufficient to change the symmetry of the resulting superlattice from hexagonal to tetragonal, highlighting the crucial importance of precise shape control in the fabrication of functional metamaterials by self-assembly of colloidal NCs.

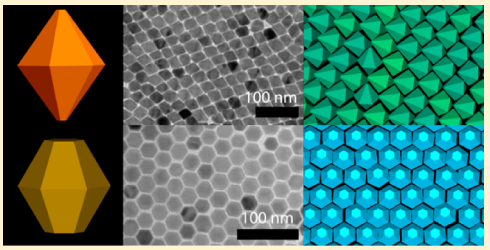

KEYWORDS: *Self-assembly, anisotropic nanocrystals, two-dimensional superlattices, Monte Carlo Simulations*

Self-assembly of colloidal nanocrystals (NCs) into ordered superlattices (NC solids) is emerging as a versatile approach to design and fabricate novel metamaterials with tailored optoelectronic properties, which are promising for a variety of devices, such as solar cells, LEDs, photodetectors, and lasers.[1−10] The collective properties of NC solids arise from the intrinsic characteristics of the building blocks and the synergistic interactions between them and can thus be engineered by a judicious choice of the colloidal NCs (composition, size, shape, surface), and the stoichiometry and spatial symmetry of the resulting self-assembled superstructure.[1−4,11,12] Nevertheless, a comprehensive set of design rules for NC superstructures has yet to emerge, although the concerted efforts of experimentalists and theoreticians worldwide have led to great advances in recent years.[1,2,13−20]

Single- and multicomponent superlattices of isotropic, nearly spherical NCs have been extensively investigated over the last two decades, producing a remarkable variety of superstructures and greatly advancing the fundamental understanding of the self-assembly process.[1,2,13−19] Recent advances in the synthesis of colloidal NCs have dramatically extended the ability to control not only the shape but also the composition of the NC, yielding a wealth of complex anisotropic NCs and heterostructured NCs.[21] Moreover, novel theoretical and simulation techniques have been developed in recent years, allowing more complex problems to be solved.[20,22−24] This has led to a surge of experimental and simulation interest on superlattices of anisotropic NC building blocks.[3,25−38] In particular, two-dimensional (2D) superstructures of anisotropic NCs are attracting increasing attention, because their properties may be substantially different from those of three-dimensional (3D) NC superstructures, making them suitable for the fabrication of functional ultrathin films and membranes that take full advantage of the shape-dependent and directional properties of anisotropic NCs. For example, nanorods have been shown to form both 2D superlattices[35−37] and 3D mesoscopic supercrystals.[38] The formation of 2D and 3D self-assembled superstructures has also been studied for other anisotropic colloidal NCs, such as nanoplates, truncated cubes, octahedrons, or octapods, both experimentally and by theory and simulation.[27−34] Although these studies provided valuable insight in the self-assembly behavior of anisotropic colloidal NCs, the driving forces behind the self-organization process are still not fully understood. For instance, the relationship between the NC shape and the symmetry of the self-assembled superlattice has not yet been investigated in detail. This is particularly relevant not only from a fundamental viewpoint, but also as a step toward the development of a framework that allows the design and fabrication of tailored NC superstructures.

Here, we report a combined experimental, theoretical, and simulation study on the self-assembly of hexagonal bipyramid- and hexagonal bifrustum-shaped ZnS NCs into 2D superlattices (see Figure 1 for a graphical illustration of the shapes). The NC

Received: December 12, 2013
Revised: January 10, 2014
Published: January 16, 2014

   dx.doi.org/10.1021/nl4046069 | *Nano Lett.* 2014, 14, 1032−1037

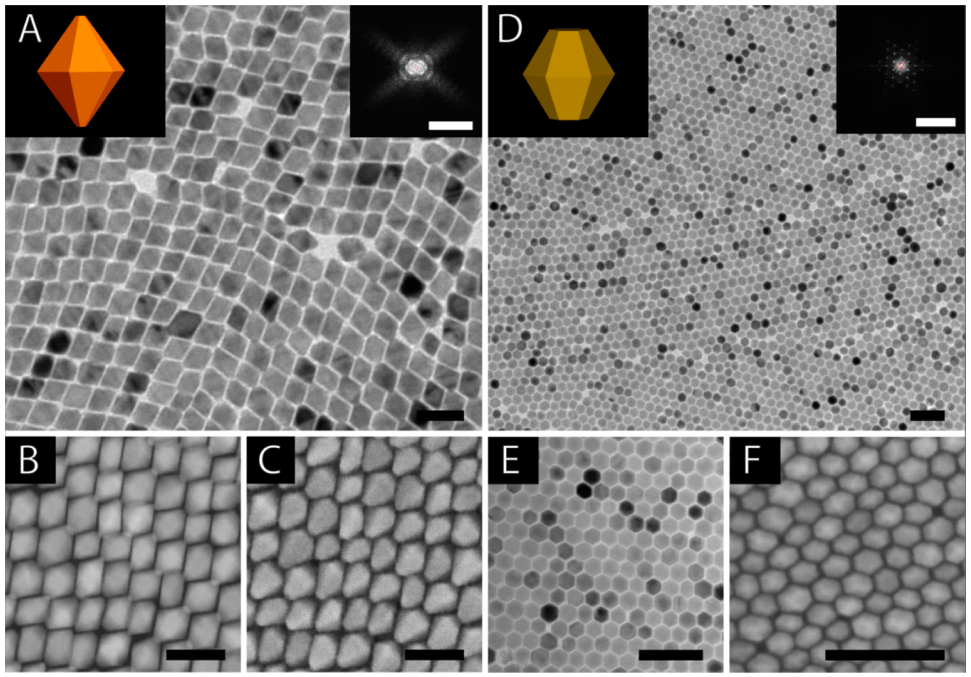

Figure 1. Electron microscopy images of self-assembled superlattices of hexagonal bipyramid-shaped ZnS NCs (A–C, TEM, dark-field STEM, SEM, respectively) and hexagonal bifrustum-shaped ZnS NCs (D–F, TEM and SEM, respectively). Fast Fourier transform (FFT) patterns of the superlattices are shown as insets in the top right corner of the corresponding TEM images (A,D). Insets in the top left corner show schematic representations of the shapes of the NCs (slightly truncated hexagonal bipyramid and hexagonal bifrustum for panel A and D, respectively). The scale bars correspond to 50 nm in A–C and to 100 nm in D–F. FFT: 0.2 nm^{-1}.

superstructures of these building blocks were obtained by slow evaporation of the solvent on a dense liquid surface (diethylene glycol). The self-assembly process was theoretically studied by modeling the NCs as hard anisotropic polyhedral nanoparticles in a planar 2D solvent-air interface. The minimum free-energy configurations (position and orientation) of individual NCs at the interface were theoretically calculated[20,39] and used in isothermal–isobaric Monte Carlo simulations[20,40,41] to determine the phase behavior of the ensemble of NCs. The agreement between experimentally observed and simulated NC superstructures is very good, showing that under the conditions prevalent in our experiments the self-assembly process is primarily driven by minimization of the interfacial free-energies and maximization of the packing density. Interestingly, the simulations show that the small truncation observed at the tips of the hexagonal bipyramid-shaped NCs has a dramatic impact on the symmetry of the resulting superlattice, changing it from hexagonal to tetragonal. This highlights the pivotal role of precise shape control in the design and fabrication of functional materials by self-assembly of colloidal NCs.

The colloidal hexagonal bipyramid- and hexagonal bifrustum-shaped ZnS NCs used in the experiments were obtained by exchange of Cu^+ for Zn^{2+} in $Cu_{2-x}S$ NCs.[42,43] The parent $Cu_{2-x}S$ NCs were synthesized by using methods adapted from the literature.[44,45] Experimental details regarding the synthesis of both $Cu_{2-x}S$ and ZnS colloidal NCs are provided in the Supporting Information. The NCs were characterized by Transmission and Scanning Electron Microscopy (TEM, SEM, Figure 1), X-ray Diffraction (XRD, Figure S1, Supporting Information) and Energy Dispersive X-ray Spectroscopy (EDS, Table S1, Supporting Information). These techniques showed that djurleite $Cu_{1.96}S$ NCs were successfully exchanged into wurtzite ZnS NCs, with preservation of size and shape. Nanoscale cation exchange (CE) is a versatile strategy for obtaining colloidal NC compositions and morphologies that would not be attainable by conventional methods.[46,47] Very often the anionic framework remains unaffected during the CE reaction, and, as a result, the shape and size of the parent NC is preserved in the product NC despite the change in composition.[46,47] CE reactions in which Cu^+ is exchanged by other metal cations with preservation of the anionic framework have been extensively investigated in copper chalcogenides, yielding NCs with metastable shapes and crystal structures.[42,46,47] This is also the case in the present work, because hexagonal bipyramid- and hexagonal bifrustum-shaped wurtzite ZnS NCs are obtained, rather than the thermodynamically stable zinc blende ZnS.

Colloidal hexagonal bipyramid and bifrustum ZnS NCs were self-assembled using the solvent evaporation technique on a liquid–air interface.[48] A solution of NCs in toluene (10^{-8} M) was drop casted on a diethylene glycol surface. Subsequently, the solvent was allowed to slowly evaporate at room temperature and the self-assembled superstructures were collected on a TEM-grid by gently dipping it in the liquid substrate. After collection, the superstructures were dried for several hours under vacuum prior to TEM imaging. Micrometer scale ordered superlattices were obtained in all cases (Figure 1). The bipyramid ZnS NCs (length, 38 nm; width, 28 nm) yielded self-assembled arrays with tetragonal symmetry (Figure 1A–C, Supporting Information Movie 1), whereas the bifrustum ZnS NCs (length, 33 nm; width, 33 nm) self-organized into hexagonal superlattices (Figure 1D–F). SEM analysis (Figure 1C) and electron tomography studies (Supporting Information Movie 1) revealed that the bipyramid NCs are all oriented in the same direction with one tip pointing upward, and the other adhered to the substrate (Figure 1C, Supporting Information Movie 1). It should be noted that the tips of the hexagonal bipyramid ZnS NCs are slightly truncated.

dx.doi.org/10.1021/nl4046069 | *Nano Lett.* 2014, 14, 1032–1037

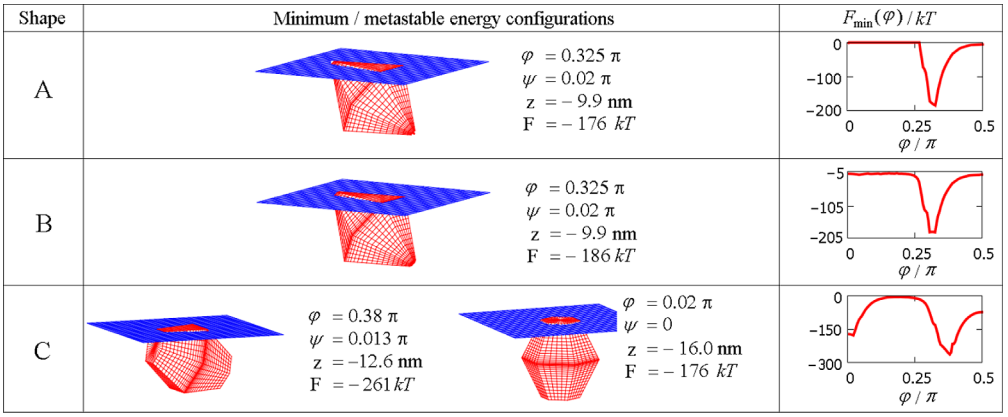

Figure 2. Minimum free-energy configurations (and their coordinates and minimal free-energy) for three particle shapes in a planar air–toluene interface as obtained from eq 1 and triangular tessellations of the surfaces, (A) perfect hexagonal bipyramid, (B) slightly truncated hexagonal bipyramid, and (C) hexagonal bifrustums. The right panels give the interfacial free-energy of the particle as a function of the polar angle φ minimized with respect to the particle height z and the internal Euler angle about the long axis of the nanoparticle, ψ.

Tip truncation is very common in colloidal NCs, because it minimizes their overall free-energy.[21] SEM showed that the bifrustum NCs can adopt multiple spatial orientations at the substrate (Figure 1F), while yielding similar hexagonal 2D TEM projections (Figure 1E). This is mainly due to the shape uniformity of the bifrustum NCs viewed from different directions. Interestingly, the parent $Cu_{1.96}S$ NCs did not form 2D superlattices under the conditions used in our experiments but formed instead small domains of 3D superstructures (Figure S2, Supporting Information). Considering that the size and shape of the parent $Cu_{1.96}S$ NCs are preserved in the product ZnS NCs, the disparity in their self-organization behavior can be ascribed to their dissimilar surfaces (both in terms of chemical composition and ligand capping), which could give rise to different inter-NC interactions and hence alter the forces driving the self-assembly process.

To understand the experimentally observed self-assembly behavior of both the product ZnS NCs and the parent $Cu_{1.96}S$ NCs, theoretical calculations and computer simulations were performed. First, the preferred orientation of the NC at a planar air–toluene interface (tension γ_{at} = 28.52 mN/m) was theoretically obtained by calculating Pieranski-type interfacial adsorption free-energies of individual NCs using a triangular tessellation technique[39] and choosing the configuration that minimizes the adsorption free-energy. The NCs were modeled as anisotropic polyhedral hard nanoparticles with the same dimensions as those experimentally observed (see above). Adsorption at the diethylene glycol (DEG)–toluene interface is neglected under the assumption that the self-assembly of the NCs occurs primarily at the air–toluene interface. This assumption is supported by a recent experimental study of the self-assembly of colloidal CdSe/CdS nanorods (NRs) by slow evaporation of toluene solutions on a DEG surface, combining in situ grazing-incidence small-angle X-ray scattering (GISAXS) and ex situ TEM, which clearly demonstrated that the superstructures are formed at the air–toluene interface.[35] Furthermore, NC adsorption at the toluene–diethylene glycol interface is likely to be negligible in comparison to that at the toluene–air interface, because the interfacial tension of air–toluene can be expected to be larger than that of toluene–diethylene glycol, as more van der Waals interactions are broken at the air–toluene interface.

Following Pieranksi,[49] we write the interfacial free-energy of a nanoparticle with its center of mass at a height z (with respect to the planar air–toluene interface) and with angles φ (the polar angle with respect to the interface normal, Figure S3, Supporting Information) and ψ (the internal Euler angle about the long axis of the nanoparticle, Figure S3, Supporting Information), as

$$F(z, \varphi, \psi) = \gamma_a S_a(z, \varphi, \psi) + \gamma_t S_t(z, \varphi, \psi) - \gamma_{at} S_{at}(z, \varphi, \psi) + \text{const} \quad (1)$$

Here S_a and S_t denote the area of the particle surface that is in contact with air and toluene, respectively, and S_{at} is the surface area taken out from the air–toluene interface by the particle. All three areas S_a, S_t, and S_{at} depend nontrivially on the position and orientation of the particle and need to be calculated numerically. The particle–toluene tension is denoted by γ_t, the particle–air tension by γ_a, and the arbitrary constant in eq 1 is chosen such that $F = 0$ for a particle that is completely immersed in toluene. The adsorption free-energy of eq 1 ignores capillary deformations and line tension contribution for simplicity. In fact, given that the total particle surface area $S_a + S_t$ is a constant, one easily checks that $F(z, \varphi, \psi)$ does not depend on γ_t and γ_a separately but only on their difference through the contact angle θ defined by Young's equation, $\cos\theta = (\gamma_a - \gamma_t)/\gamma_{at}$ = 0.8, where the numerical value is an estimate based on the observed favorable (low free-energy) configurations (see Figure S3, Supporting Information). It should be noted that although ignoring capillary deformations of the toluene–air interface gives rise to a violation of the force balance on the toluene–air–particle contact line, we expect this to have a negligible effect on the optimal configuration since the sharp edges of the flat facet adsorbed to the interface cause a rapid variation of the surface curvature to which the air–toluene interface can adapt without any substantial deformation.

Using a triangular tessellation technique to calculate the surface areas S_a, S_t, and S_{at}, we obtain the equilibrium configuration from minimizing F with respect to the particle configuration. For three nanoparticle shapes of interest, Figure 2 shows these equilibrium configurations, as well as their coordinates and free-energies as a function of the polar angle φ (minimized with respect to z and the internal angle ψ). The

dx.doi.org/10.1021/nl4046069 | Nano Lett. 2014, 14, 1032–1037

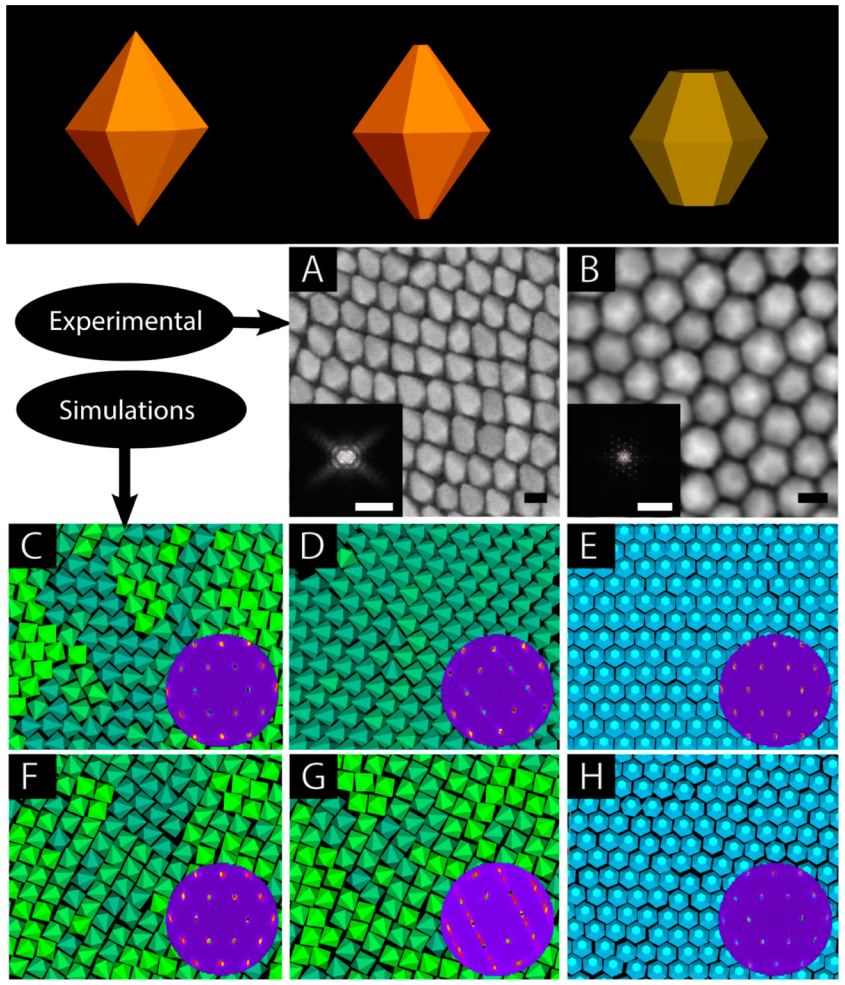

Figure 3. Top panel: Schematics of the particle geometries used in the Monte Carlo simulations. Second row from top: SEM images of self-assembled superlattices of (A) hexagonal bipyramid-shaped ZnS NCs, and (B) hexagonal bifrustum-shaped ZnS NCs. The insets give the FFT patterns of the superlattices. The scale bars correspond to 20 nm (0.2 nm^{-1} in the insets). Bottom two rows. Snapshots of the isothermal−isobaric Monte Carlo simulations showing the various structures that form during the 2D self-assembly of hexagonal bipyramids (C,D,F,G) and hexagonal bifrustums (E,H) adhered to an air−toluene interface. The corresponding reciprocal space patterns of the center of mass of the particles in the simulated NC superlattice are also displayed (bottom right insets). The orientation of the particles with respect to the interface is fixed based on the equilibrium configurations obtained from the interfacial free-energy calculations (see Figure 2). The relative orientation of the particles is color coded. A movie file showing various stages of the NC self-assembly process during the simulation runs is provided as Supporting Information (Movie 2). (C−E) Simulation snapshots at a reduced density $\rho^* = \rho v^{2/3} = 0.69$ with v as the particle volume. (F−H) Simulation snapshots at $\rho^* = 0.65$.

perfect hexagonal bipyramid has minimum free-energy when one of its triangular facets is completely adhered to the interface (Figure 2A). For this configuration, a local minimum of ca. $-200\ k_BT$ is found. It is interesting to note that the particle remains completely immersed in the liquid phase, except for the facet that is adhered to the interface (whereas the particle pays a free-energy penalty of $F \approx 10^4\ k_BT$ if it is completely in air). The colloidal NCs used in the self-assembly experiments are, however, not perfect hexagonal bipyramids, but instead have slightly truncated tips (5% of their length). Nevertheless, according to our calculation this small truncation does not affect the single-particle equilibrium configuration at the interface, which remains essentially the same as that of a perfect hexagonal bipyramid (Figure 2B). By contrast, according to our calculations a hexagonal bifrustum nanoparticle has two possible equilibrium configurations in which either 1 of the 12 trapezoidal facets or 1 of the 2 hexagonal facets is adhered to the interface (Figure 2C). Both free-energy minima are sufficiently deep to make the adhesion irreversible (Figure 2C), and consequently the hexagonal bifrustum nanoparticles have multiple options for interfacial adhesion.

Once the equilibrium adsorption configurations of individual nanoparticles at the air−toluene interface are theoretically determined, we predict the self-assembled structures by using the floppy-box Monte Carlo (FBMC) method[40,41] in combination with the separating-axis-based overlap algorithm.[50] In the FBMC method, we perform Monte Carlo simulations in the isothermal−isobaric ensemble (*NPT*) and compress the system from the isotropic fluid phase to the solid phase using a variable shape of the simulation box. The immersion depth z and the polar angle φ of the nanoparticle with respect to the air−toluene interface are kept fixed according to the values determined for the equilibrium adsorption configurations, and the particles are only allowed to translate and rotate in the plane of the interface. Because of the symmetry of the hexagonal bifrustums (ca. 33 nm in all directions), the orientation of the NC is not important for the overall self-assembly behavior, because the NC can occupy a hexagonal site

dx.doi.org/10.1021/nl4046069 | *Nano Lett.* 2014, 14, 1032−1037

in the array regardless of whether a trapezoidal or hexagonal facet is adsorbed to the interface (Figure S4, Supporting Information). Therefore, for simplicity only the hexagonal adhered surface is considered in the FBMC simulations. The volume of the nanoparticles v is set to unity in all cases.

Subsequently, we use the predicted self-assembled structures in Monte Carlo simulations to determine the phase behavior of an ensemble of nanoparticles. To this end, we calculate the equations of state in Monte Carlo simulations, which we show in Figure S5 (Supporting Information). A movie file showing the simulated self-assembly process at various stages during the *NPT* compression runs is provided as Supporting Information (Supporting Movie 2). The change in the color of the particles depicts the orientation of the particles. The crystal structure can be determined from the reciprocal space pattern of the center of mass of the particles in the simulated NC superstructure. Figure 3 shows the reciprocal space patterns and the real space configurations of the NC superlattices formed during the FBMC simulations at two different reduced densities $\rho^* = \rho v^{2/3} = 0.65$ and 0.69 with v as the particle volume, $\rho = N/A$ is the areal number density, N is the number of particles, and A is the surface area of the interface. The experimentally observed NC superlattices are also included for comparison (Figure 3A–B). The simulations show that perfect hexagonal bipyramids crystallize via a first-order phase transition with coexisting densities $\rho^* \approx 0.56$ and 0.57 into a hexagonal superlattice (Figure 3C). Hexagonal bifrustums also crystallize via a first-order transition from the isotropic fluid into a hexagonal lattice with coexisting densities $\rho^* \approx 0.50$ and 0.52 (Figure 3E). In contrast, slightly truncated bipyramids show a weak first-order transition from the isotropic phase to a tetragonal phase around $\rho^* \approx 0.58$ (Figure 3D). This is remarkable because the equilibrium configuration of the single NC adhered to the air–toluene interface was not significantly affected by the truncation (see above, Figure 2). This can be rationalized by considering that the truncation allows the NCs to come in closer proximity, thereby leading to a higher packing density, and hence a tetragonal rather than hexagonal lattice.

The agreement between the simulated and experimentally observed self-assembled 2D NC superlattices (Figure 3) is very good, indicating that the self-assembly process of the ZnS NCs is driven primarily by minimization of the interfacial free-energies and maximization of the packing densities. The inability of the parent $Cu_{1.96}S$ NCs to form 2D superlattices under the same conditions as used for the product ZnS NCs can be thus attributed to the presence of additional inter-NC interactions that disrupt the self-assembly process by modifying the interfacial tensions and/or introducing attractive/repulsive potentials. Considering that the size and shape of the ZnS and $Cu_{1.96}S$ NCs are the same, the additional interactions must be due to the different surfaces of the two types of NCs, since the $Cu_{1.96}S$ NCs are capped by alkylthiols, while the ZnS NCs are likely capped by oleylamine and Cl. Indeed, superlattices were no longer formed after the ligands coating the ZnS NCs were exchanged to 1-dodecanethiol (Figure S6A, Supporting Information) or trioctyl phosphine (Figure S6C, Supporting Information), while an excess of oleylamine did not affect the formation of the superlattices (Figure S6B, Supporting Information).

In conclusion, our work shows that micrometer scale 2D superlattices of colloidal hexagonal bipyramid- and hexagonal bifrustum-shaped ZnS NCs can be obtained by self-assembly at the liquid–air interface. The self-assembly behavior is well described by a combination of theoretical adsorption free-energy calculations and Monte Carlo simulations, which shows that the superlattice formation is driven primarily by minimization of the interfacial free-energies and maximization of the packing densities. Moreover, our results show that truncation of the tips of hexagonal bipyramids by as little as 5% is sufficient to change the symmetry of the resulting superlattice from hexagonal to tetragonal. This demonstrates that precise shape control is of crucial importance in the fabrication of functional materials by self-assembly of colloidal NCs. From this perspective, the strategy developed in our work is very promising, since colloidal $Cu_{2-x}A$ (A = S, Se, Te) NCs can be synthesized in a plethora of different shapes,[44,45] and can easily be converted into NCs of other metal chalcogenides with preservation of size and shape by using cation exchange.[42,43,46,47] Moreover, it has recently been demonstrated that Zn^{2+} in Zn chalcogenides can also be exchanged for other cations (e.g., Cd^{2+}, Mn^{2+}).[51−53] The work described here may thus provide a versatile design and fabrication route for tailored 2D superlattices of anisotropic NCs of metal chalcogenides in which cation exchange reactions are used to convert self-assembled superlattices of zinc chalcogenide NCs into different materials, while preserving the size and shape of the NC building blocks as well as the symmetry and long-range order of the superstructure. From a theoretical and modeling perspective, it is very comfortable to note that the relatively simple Pieranski potential of eq 1 combined with Monte Carlo simulations actually has quantitative predictive power, which may be further exploited in the study of other particle shapes and material parameters.

■ ASSOCIATED CONTENT

Ⓢ Supporting Information

Experimental methods, additional figures, an electron tomography movie file showing a series of tilted TEM images of a self-assembled superstructure of hexagonal bipyramid-shaped ZnS NCs, and a movie file showing various stages of the NC self-assembly process during the isothermal–isobaric Monte Carlo simulation runs. The orientation of the NCs in the simulation movie is color coded, so that particles oriented in the same direction have the same color. This material is available free of charge via the Internet at http://pubs.acs.org.

■ AUTHOR INFORMATION

Corresponding Authors

*E-mail: (C.d.M.D.) c.demello-donega@uu.nl.
*E-mail: (M.D.) m.dijkstra1@uu.nl.

Notes

The authors declare no competing financial interest.

■ ACKNOWLEDGMENTS

W.v.d.S. and C.d.M.D. acknowledge financial support from the division of Chemical Sciences (CW) of The Netherlands Organization for Scientific Research (NWO) under Grant ECHO.712.012.001. A.P.G and M.D. acknowledge financial support from an NWO-VICI grant. This work is part of the D-ITP consortium, a program of the NWO that is funded by the Dutch Ministry of Education, Culture, and Science (OCW).

■ REFERENCES

(1) Talapin, D. V.; Lee, J.; Kovalenko, M. V.; Shevchenko, E. V. *Chem. Rev.* **2010**, *110*, 389–458.

(2) Vanmaekelbergh, D. *Nano Today* **2011**, *6*, 419−437.
(3) Paik, T.; Murray, C. *Nano Lett.* **2013**, *13*, 2952−2956.
(4) Nie, Z.; Petukhova, A.; Kumacheva, E. *Nat. Nanotechnol.* **2010**, *5*, 15−25.
(5) Shirasaki, Y.; Supran, G. J.; Bawendi, M. G.; Bulović, V. *Nat. Photonics* **2013**, *7*, 13−23.
(6) Sun, L.; Choi, J. J.; Stachnik, D.; Bartnik, A. C.; Hyun, B. R.; Malliaras, G. G.; Hanrath, T.; Wise, F. W. *Nat. Nanotechnol.* **2012**, *7*, 369−373.
(7) Pisanello, F.; Martiradonna, L.; Spinicelli, P.; Fiore, A.; Hermier, J. P.; Manna, L.; Cingolani, R.; Giacobino, E.; De Vittorio, M.; Bramati, A. *Superlattices Microstruct.* **2010**, *47*, 165−169.
(8) Talgorn, E.; Gao, Y.; Aerts, M.; Kunneman, L. T.; Schins, J. M.; Sevenije, T. J.; van Huis, M. A.; van der Zant, H. S. J.; Houtepen, A. J.; Siebbeles, L. D. A. *Nat. Nanotechnol.* **2011**, *6*, 733−739.
(9) Tang, J.; Kemp, K. W.; Hoogland, S.; Jeong, K. S.; Liu, H.; Levina, L.; Furukawa, M.; Wang, X.; Debnath, R.; Cha, D.; Chou, K. W.; Fischer, A.; Amassian, A.; Asbury, J. B.; Sargent, E. H. *Nat. Mater.* **2011**, *10*, 765−771.
(10) Ip, A. H.; Thon, S. M.; Hoogland, S.; Voznyy, O.; Zhitomirsky, D.; Debnath, R.; Levina, L.; Rollny, L. R.; Carey, G. H.; Fischer, A.; et al. *Nat. Nanotechnol.* **2012**, *7*, 577−582.
(11) Wang, R. Y.; Feser, J. P.; Lee, J.-S.; Talapin, D. V; Segalman, R.; Majumdar, A. *Nano Lett.* **2008**, *8*, 2283−2288.
(12) Kang, Y.; Ye, X.; Chen, J.; Qi, L.; Diaz, R. E.; Doan-Nguyen, V.; Xing, G.; Kagan, C. R.; Li, J.; Gorte, R. J.; Stach, E. A.; Murray, C. B. *J. Am. Chem. Soc.* **2013**, *135*, 1499−1505.
(13) Urban, J. J.; Talapin, D. V; Shevchenko, E. V; Kagan, C. R.; Murray, C. B. *Nat. Mater.* **2007**, *6*, 115−121.
(14) Shevchenko, E. V; Talapin, D. V; Kotov, N. A.; O'Brien, S.; Murray, C. B. *Nature* **2006**, *439*, 55−59.
(15) Heath, J. R. *Nature* **2007**, *445*, 492−493.
(16) Boneschanscher, M. P.; Evers, W. H.; Qi, W.; Meeldijk, J. D.; Dijkstra, M.; Vanmaekelbergh, D. *Nano Lett.* **2013**, *13*, 1312−1316.
(17) Evers, W. H.; Goris, B.; Bals, S.; Casavola, M.; de Graaf, J.; Roij, R.; Van Dijkstra, M.; Vanmaekelbergh, D. *Nano Lett.* **2012**, *13*, 2317−2323.
(18) Chen, Z.; O'Brien, S. *ACS Nano* **2008**, *2*, 1219−1229.
(19) Grzelczak, M.; Vermant, J.; Furst, E.; Liz-Marzán, L. *ACS Nano* **2010**, *4*, 3591−3605.
(20) Gantapara, A. P.; de Graaf, J.; van Roij, R.; Dijkstra, M. *Phys. Rev. Lett.* **2013**, *111*, 015501.
(21) Donega, C. d. M. *Chem. Soc. Rev.* **2011**, *40*, 1512−1546.
(22) Torquato, S.; Jiao, Y. *Nature* **2009**, *460*, 876.
(23) Nguyen, T. D.; Jankowski, E.; Glotzer, S. C. *ACS Nano* **2011**, *5*, 8892−8903.
(24) Sinkovits, D. W.; Luijten, E. *Nano Lett.* **2012**, *12*, 1743−1748.
(25) Quan, Z.; Fang, J. *Nano Today* **2010**, *5*, 390−411.
(26) Glotzer, S. C.; Solomon, M. J. *Nat. Mater.* **2007**, *6*, 557−562.
(27) Reifsnyder, D. C.; Ye, X.; Gordon, T. R.; Song, C.; Murray, C. B. *ACS Nano* **2013**, *7*, 4307−4315.
(28) Gordon, T. R.; Paik, T.; Klein, D. R.; Naik, G. V; Caglayan, H.; Boltasseva, A.; Murray, C. B. *Nano Lett.* **2013**, *13*, 2857−2863.
(29) Qi, W.; de Graaf, J.; Qiao, F.; Marras, S.; Manna, L.; Dijkstra, M. *Nano Lett.* **2012**, *12*, 5299−5303.
(30) Miszta, K.; de Graaf, J.; Bertoni, G.; Dorfs, D.; Brescia, R.; Marras, S.; Ceseracciu, L.; Cingolani, R.; van Roij, R.; Dijkstra, M.; Manna, L. *Nat. Mater.* **2011**, *10*, 872−876.
(31) Du, W.; Qian, X.; Ma, X.; Gong, Q.; Cao, H.; Yin, J. *Chemistry* **2007**, *13*, 3241−3247.
(32) Evers, W. H.; Goris, B.; Bals, S.; Casavola, M.; de Graaf, J.; van Roij, R.; Dijkstra, M.; Vanmaekelbergh, D. *Nano Lett.* **2013**, *13*, 2317−2323.
(33) Baumgardner, W. J.; Whitham, K.; Hanrath, T. *Nano Lett.* **2013**, *13*, 3225−3231.
(34) Ye, X.; Chen, J.; Engel, M.; Millan, J. A.; Li, W.; Qi, L.; Xing, G.; Collins, J. E.; Kagan, C. R.; Li, J.; Glotzer, S. C.; Murray, C. B. *Nat. Chem.* **2013**, *5*, 466−473.
(35) Pietra, F.; Rabouw, F. T.; Evers, W. H.; Byelov, D. V; Petukhov, A. V; de Mello Donega, C.; Vanmaekelbergh, D. *Nano Lett.* **2012**, *12*, 5515−5523.
(36) Carbone, L.; Nobile, C.; De Giorgi, M.; Sala, F.; Della Morello, G.; Pompa, P.; Hytch, M.; Snoeck, E.; Fiore, A.; Franchini, I. R.; Nadasan, M.; Silvestre, A. F.; Chiodo, L.; Kudera, S.; Cingolani, R.; Krahne, R.; Manna, L. *Nano Lett.* **2007**, *7*, 2942−2950.
(37) Rivest, J. B.; Swisher, S. L.; Fong, L. K.; Zheng, H.; Alivisatos, A. P. *ACS Nano* **2011**, *5*, 3811−3816.
(38) Wang, T.; Zhuang, J.; Lynch, J.; Chen, O.; Wang, Z.; Wang, X.; LaMontagne, D.; Wu, H.; Wang, Z.; Cao, Y. C. *Science* **2012**, *338*, 358−363.
(39) De Graaf, J.; Dijkstra, M.; van Roij, R. *J. Chem. Phys.* **2010**, *132*, 164902.
(40) De Graaf, J.; Filion, L.; Marechal, M.; van Roij, R.; Dijkstra, M. *J. Chem. Phys.* **2012**, *137*, 214101.
(41) Filion, L.; Marechal, M.; van Oorschot, B.; Pelt, D.; Smallenburg, F.; Dijkstra, M. *Phys. Rev. Lett.* **2009**, *103*, 188302.
(42) Li, H.; Zanella, M.; Genovese, A.; Povia, M.; Falqui, A.; Giannini, C.; Manna, L. *Nano Lett.* **2011**, *11*, 4964−4970.
(43) Zhao, Y.; Pan, H.; Lou, Y.; Qiu, X.; Zhu, J.; Burda, C. *J. Am. Chem. Soc.* **2009**, *131*, 4253−4261.
(44) Kuzuya, T.; Tai, Y.; Yamamuro, S.; Sumiyama, K. *Sci. Technol. Adv. Mater.* **2005**, *6*, 84−90.
(45) Li, W.; Shavel, A.; Guzman, R.; Rubio-Garcia, J.; Flox, C.; Fan, J.; Cadavid, D.; Ibáñez, M.; Arbiol, J.; Morante, J. R.; Cabot, A. *Chem. Commun.* **2011**, *47*, 10332−10334.
(46) Rivest, J. B.; Jain, P. K. *Chem. Soc. Rev.* **2013**, *42*, 89−96.
(47) Beberwyck, B. J.; Surendranath, Y.; Alivisatos, A. P. *J. Phys. Chem. C* **2013**, *117*, 19759−19770.
(48) Dong, A.; Chen, J.; Vora, P. M.; Kikkawa, J. M.; Murray, C. B. *Nature* **2010**, *466*, 474−477.
(49) Pieranski, P. *Phys. Rev. Lett.* **1980**, *45*, 569−572.
(50) Eberly, D. Intersection of Convex Objects: The Method of Separating Axes, http://www.geometrictools.com/ (accessed April 2013).
(51) Eilers, J.; Groeneveld, E.; Donega, C. d. M.; Meijerink, A. *J. Phys. Chem. Lett.* **2012**, *3*, 1663−1667.
(52) Groeneveld, E.; van Berkum, S.; van Schooneveld, M. M.; Gloter, A.; Meeldijk, J. D.; van den Heuvel, D. J.; Gerritsen, H. C.; Donega, C. d. M. *Nano Lett.* **2012**, *12*, 749−757.
(53) Groeneveld, E.; Witteman, L.; Lefferts, M.; Ke, X.; Bals, S.; van Tendeloo, G.; Donega, C. d. M. *ACS Nano* **2013**, *7*, 7913−7930.

SUPPORTING INFORMATION

Self-Assembly of Colloidal Hexagonal Bipyramid- and Bifrustum-shaped ZnS Nanocrystals into Two-Dimensional Superstructures

Ward van der Stam†, Anjan P. Gantapara§, Quinten A. Akkerman†, Giuseppe Soligno§, Johannes D. Meeldijk‖, René van Roij‡, Marjolein Dijkstra§, and Celso de Mello Donega*†*

†Condensed Matter and Interfaces and §Soft Condensed Matter, Debye Institute for Nanomaterials Science, Utrecht University, 3508 TA Utrecht, The Netherlands

‡Institute for Theoretical Physics, Utrecht University, Leuvenlaan 4, 3584 CE Utrecht, The Netherlands

‖Electron Microscopy Utrecht, Utrecht University, 3584 CH Utrecht, The Netherlands

Corresponding Authors: *c.demello-donega@uu.nl, *m.dijkstra1@uu.nl

Methods

Synthesis.

Colloidal hexagonal bipyramid-shaped $Cu_{2-x}S$ NCs were synthesized based on a modification of the method described by Kuzuya *et al.*[1] Typically, 1.0 mmol CuCl and 0.5 mmol $SnBr_4$ were mixed in 8 mL 1-dodecanethiol (DDT) and 2 mL oleylamine (OLAM) and gradually heated to 225 °C. At first, a turbid white suspension was obtained at RT. The solution turned turbid yellow around 80 °C, and clear yellow at 130 °C. When the temperature reached 225 °C, the solution turned brown/black, indicating the formation and growth of $Cu_{2-x}S$ NCs. The solution was maintained at this temperature for one hour. Finally, the nanoparticles were washed by adding methanol/butanol solution as anti-solvent, followed by centrifugation and redispersion in toluene. This cycle was repeated 3 times.

Colloidal hexagonal bifrustum-shaped $Cu_{2-x}S$ NCs were synthesized according to Li *et al.*[2] In a typical synthesis, 8 mmol of $CuCl_2 \cdot 2H_2O$ and 12 g OLAM were heated to 200 °C under nitrogen flow. After one hour the clear dark brown solution was cooled to 180 °C and 2 mL tert-butyl disulfide (10 mmol) was swiftly injected. The solution was re-heated to 200 °C and after 40 minutes of growth the reaction mixture was cooled. Subsequently, the NCs were washed three times with a methanol/butanol solution as anti-solvent, and redispersed in toluene.

Cation exchange reactions of Cu^+ for Zn^{2+} were performed as described by Li *et al.*[3] First, 1 mmol $ZnCl_2$ was dissolved in 3 mL 1-octadecene and 2 mL OLAM (both previously degassed) at 250 °C. Subsequently, $Cu_{2-x}S$ NCs dispersed in trioctylphosphine (TOP) were injected at that temperature. The mixture was allowed to react for 5 min. under heating and stirring, after which the temperature was lowered to 70 °C, followed by the addition of several mL´s toluene. The final sample was precipitated by adding a methanol/butanol solution. The NCs were isolated by centrifugation and redispersed in toluene. This cycle was repeated twice.

Self-assembled NC superlattices were obtained by the liquid-air interface method, described by Chen *et al.*[4] In this method, a concentrated NC solution is brought onto a very dense liquid surface (di-ethylene glycol). The toluene is allowed to slowly evaporate at room temperature, resulting in the formation of a continuous membrane at the liquid-air interface. These membranes were transferred to a TEM-grid by dipping it in the liquid substrate and subsequently the grid was dried overnight prior to further investigation.

Ligand exchange reactions were performed by dispersing the NCs with the native capping ligands in an excess of the new ligand at ~100 °C for several hours. The NCs were subsequently precipitated by the addition of methanol/butanol solution, isolated by centrifugation, and redispersed in toluene.

Characterization

X-Ray Diffraction (XRD) patterns were obtained by using a PW 1729 Philips diffractometer, equipped with a Cu K_α X-ray source (λ=1.5418 Å). Samples for XRD analysis were prepared by depositing purified NCs on a Si wafer substrate under inert atmosphere. The purification procedure consisted of precipitating the NCs from a solution of NCs in toluene by adding anhydrous methanol (1:1 volume ratio). The sediment was isolated by centrifugation (3000 rpm, 15 min) and redispersed in chloroform. The concentrated solution of NCs was dropcasted op the Si wafer and the chloroform was allowed to evaporate at RT, resulting in a concentrated NC solid.

Transmission Electron Microscopy (TEM) and Energy Dispersive X-Ray Spectroscopy (EDS). TEM and EDS measurements were performed on a Tecnai20F (FEI) microscope equipped with a Field Emission Gun, a Gatan 694 CCD camera and an EDAX spectrometer. The microscope was operated at 200 kV. Acquisition time for EDS measurements was 30 s. Samples for TEM imaging were prepared by dipping a carbon coated polymer film copper grid (300 mesh) into a self-assembled thin film on a dense di-ethylene glycol surface after evaporation of the solvent (toluene). The TEM-grids were dried overnight prior to imaging.

Table S1. Elemental composition of the hexagonal bipyramid- and bifrustum-shaped ZnS NCs obtained by Cu^{+} for Zn^{2+} cation exchange in $Cu_{1.96}S$ NCs. The elements were quantified by Energy Dispersive X-Ray Spectroscopy (EDS). To ensure that the elemental concentrations were statistically valid and representative of the whole NC ensemble, EDS analyses were performed on wide areas (~10^4-10^5 nm^2, ~1000 to 5000 NCs), and averaged over several observation spots.

Sample ID	Zn:S:Cu
Bipyramids	0.99:1.00:0.05
Bifrustums	1.11:1.00:0.01

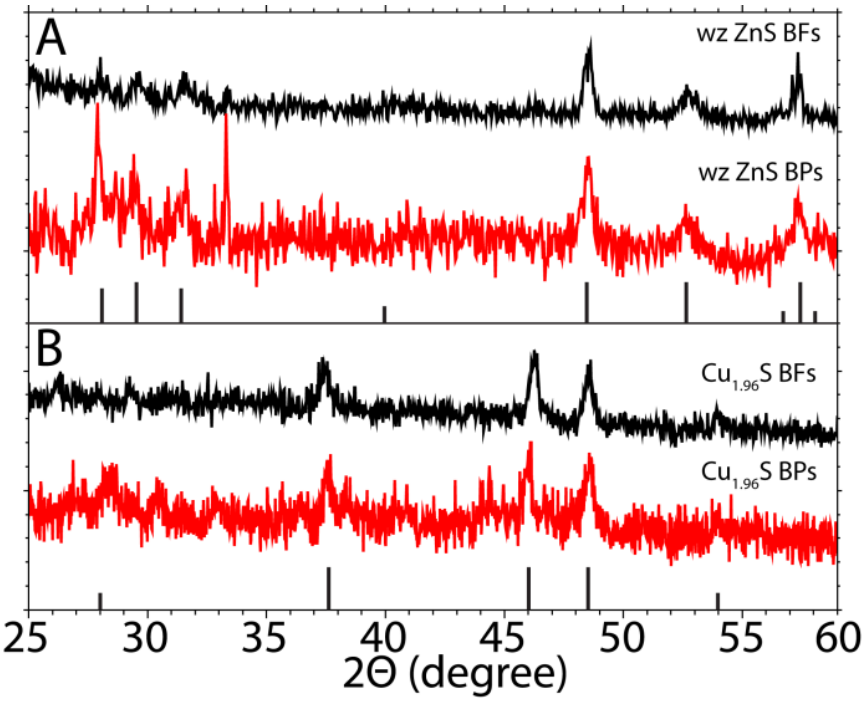

Figure S1. X-ray Diffraction patterns, indicating that (A) wurtzite ZnS hexagonal bipyramids (BPs) and bifrustums (BFs) were successfully synthesized from (B) djurleite $Cu_{1.96}S$ hexagonal BPs and BFs by Cu^{+} for Zn^{2+} cation exchange. Reference bars are from JCPDS card no. [05-0492] and [20-0365] for wurtzite ZnS and djurleite $Cu_{1.96}S$, respectively.

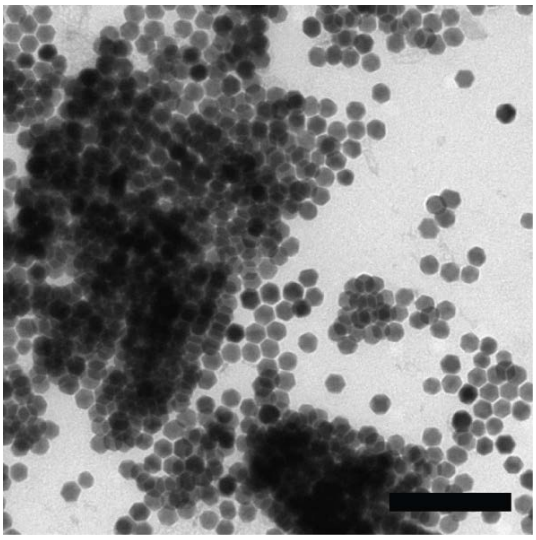

Figure S2. Self-assembled superstructures obtained from hexagonal bifrustum-shaped $Cu_{1.96}S$ NCs, capped with alkylthiols. Scale bar corresponds to 200 nm.

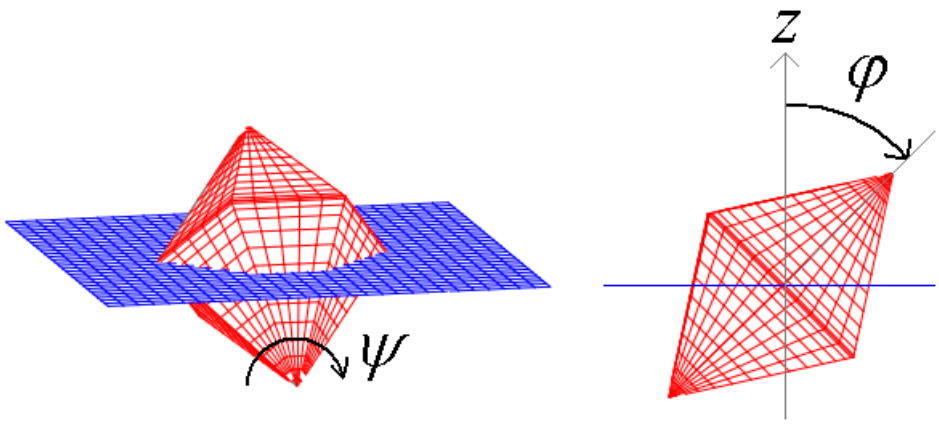

Figure S3. Definition of different orientational angles of the hard particles with respect to the interface (Equation 1 of the main text).

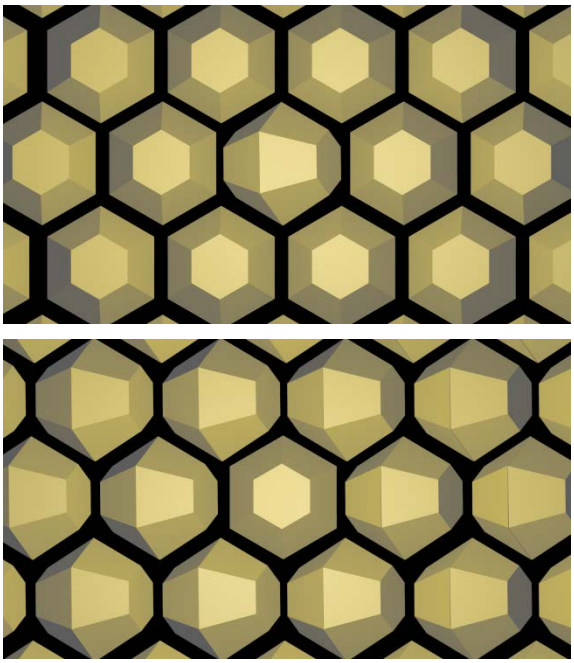

Figure S4. Schematic showing the different orientations of the hexagonal bifrustums at the interface, indicating that the NC can occupy a hexagonal site in the array regardless of whether a trapezoidal or hexagonal facet is adsorbed to the interface. Therefore, solely adsorption with the hexagonal facet is considered for simplicity in the FBMC simulations.

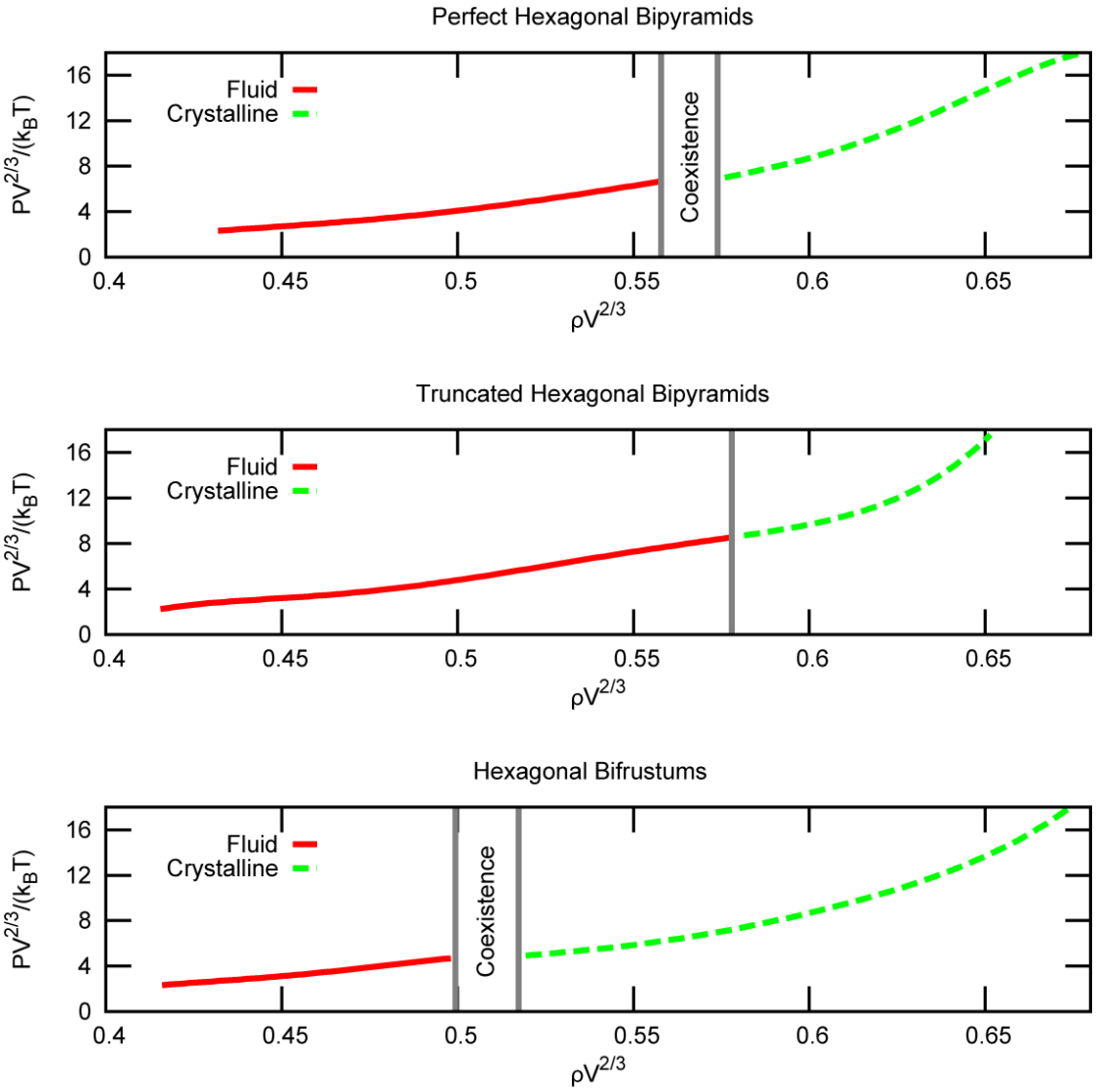

Figure S5. Equations of State (EOS), reduced pressure $P^* = \beta P v^{2/3}$ *versus* number density $\rho^* = \rho v^{2/3}$, obtained using floppy-box Monte Carlo (FBMC) simulations with $\beta = 1/k_B T$ as the inverse temperature. Perfect hexagonal bipyramids (BPs) undergo a first-order transition with coexisting densities $\rho^* \approx 0.56$ and 0.57 from the isotropic fluid phase to a hexagonal lattice, while slightly truncated hexagonal BPs show a weak first-order transition around $\rho^* \approx 0.58$ from an isotropic phase to a tetragonal lattice. Hexagonal bifrustums (BFs) crystallize *via* a first-order phase transition from the isotropic fluid into a hexagonal lattice with coexisting densities $\rho^* \approx 0.50$ and 0.52.

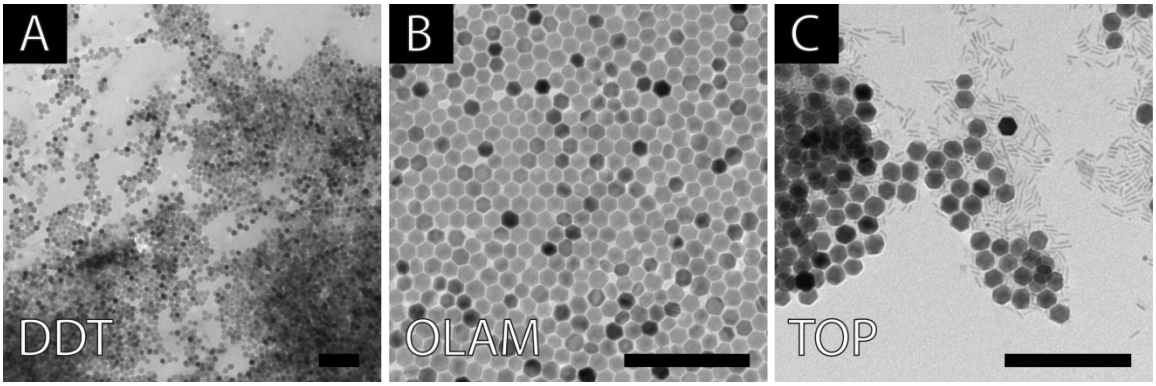

Figure S6. TEM images of the NC solids obtained from self-assembly experiments using hexagonal bifrustum ZnS NCs with different capping ligands: 1-dodecanethiol (DDT, A), additional oleylamine (OLAM, B), and trioctyl phosphine (TOP, C). These experiments show that self-assembled superlattices of ZnS NCs were only obtained when OLAM is used as the capping ligand. Scale bars correspond to 200 nm.

SUPPORTING REFERENCES

(1) Kuzuya, T.; Tai, Y.; Yamamuro, S.; Sumiyama, K. *Sci. Technol. Adv. Mater.* **2005**, *6*, 84–90.

(2) Li, W.; Shavel, A.; Guzman, R.; Rubio-Garcia, J.; Flox, C.; Fan, J.; Cadavid, D.; Ibáñez, M.; Arbiol, J.; Morante, J. R.; Cabot, A. *Chem. Commun.* **2011**, *47*, 10332–10334.

(3) Li, H.; Zanella, M.; Genovese, A.; Povia, M.; Falqui, A.; Giannini, C.; Manna, L. *Nano Lett.* **2011**, *11*, 4964–4970.

(4) Chen, J.; Dong, A.; Cai, J.; Ye, X.; Kang, Y.; Kikkawa, J. M.; Murray, C. B. *Nano Lett.* **2010**, *10*, 5103–5108